

Factored Levenberg–Marquardt for Diffeomorphic Image Registration: An efficient optimizer for FireANTs

Rohit Jena

*Department of Computer and Information Science
University of Pennsylvania
Philadelphia, PA 19104, USA*

rjena@seas.upenn.edu

Pratik Chaudhari

*Department of Electrical and Systems Engineering
University of Pennsylvania
Philadelphia, PA 19104, USA*

pratikac@seas.upenn.edu

James C. Gee

*Department of Radiology & Penn Image Computing and Science Laboratory (PICSL)
Perelman School of Medicine, University of Pennsylvania
Philadelphia, PA 19104, USA*

gee@upenn.edu

Abstract

FireANTs (Jena et al., 2026) introduced a novel Eulerian descent method for plug-and-play behavior with arbitrary optimizers adapted for diffeomorphic image registration as a test-time optimization problem, with a GPU-accelerated implementation. FireANTs uses Adam as its default optimizer for fast and more robust optimization. However, Adam requires storing state variables (i.e. momentum and squared-momentum estimates), each of which can consume significant memory, prohibiting its use for significantly large images. In this work, we propose a *modified* Levenberg–Marquardt (LM) optimizer that requires only a single scalar damping parameter as optimizer state, that is adaptively tuned using a trust region approach. The resulting optimizer reduces memory by up to 24.6% for large volumes, and retaining performance across all four datasets. A single hyperparameter configuration tuned on brain MRI transfers without modification to lung CT and cross-modal abdominal registration, matching or outperforming Adam on three of four benchmarks. We also perform ablations on the effectiveness of using Metropolis-Hastings style rejection step to prevent updates that worsen the loss function.

1 Introduction

FireANTs (Jena et al., 2026) frames diffeomorphic image registration as GPU-accelerated test-time optimization: a displacement field $\mathbf{u} : \Omega \rightarrow \mathbb{R}^d$ is optimized by minimizing

$$\mathcal{L}(\mathbf{u}) = \mathcal{L}_{\text{sim}}(F, M \circ \phi) + \mathcal{R}(\mathbf{u}), \quad (1)$$

where \mathcal{L}_{sim} is an image similarity loss and \mathcal{R} regularizes the deformation $\phi = \text{Id} + \mathbf{u}$. Adam (Kingma & Ba, 2015) is the default optimizer, and it works well. But Adam is a quasi-second-order method: it exploits gradient *history* through exponential moving averages. These moving averages can consume significant additional memory and runtime proportional to the voxels in the image, limiting their use for datasets with large volumes. Although Adam is much cheaper than other second-order methods like L-BFGS (Liu & Nocedal, 1989), it could still introduce a significant overhead for large images. This motivates the use of a more efficient second-order method that is not as memory-intensive.

Levenberg–Marquardt (LM) (Levenberg, 1944; Marquardt, 1963) is a well-known algorithm: a damped Gauss-Newton step that interpolates between Newton’s method (fast near optima) and gradient descent

(robust far from them). However, the full $\mathbf{J}^\top \mathbf{J}$ Hessian is intractable for dense warp fields due to its scale: a 192^3 displacement field has $\sim 5 \times 10^{13}$ parameters. We show that the local structure of the registration loss makes a *per-voxel* rank-1 Hessian factorization both principled and sufficient, yielding a closed-form update that is as cheap to compute as Adam yet demonstrates second-order behavior.

To evaluate our approach, we conduct experiments on four publicly available benchmarks: brain MRI (LUMIR and OASIS), lung CT (NLST), and cross-modal abdominal MR-to-CT registration (Abdomen-L2R). We compare our factored Levenberg–Marquardt (LM) optimizer against Adam, the default optimizer in FireANTs, using the same registration framework and similarity metric across datasets, showing slight improvements in performance without recording any additional state. Our ablation on synthetically generated volumes demonstrate that LM not only reduces memory consumption by up to 24.6% for large volumes, but also matches or surpasses Adam in registration accuracy using a single hyperparameter configuration transferred across imaging modalities and organs. We additionally provide ablations that highlight the effectiveness of a Metropolis-Hastings-style rejection step, which prevents loss-increasing updates and contributes to the optimizer’s stability.

2 Factored Levenberg–Marquardt for Warp Fields

2.1 Compositive Diffeomorphic Updates with Adaptive Optimization

FireANTs maintains diffeomorphism throughout optimization via a compositive update rule. Given a velocity $\mathbf{v}^{(t)}$ produced by the optimizer, the warp is updated as

$$\mathbf{u}^{(t+1)} = \epsilon \mathbf{v}^{(t)} + \mathbf{u}^{(t)} \circ (\text{Id} + \epsilon \mathbf{v}^{(t)}), \quad (2)$$

where ϵ is a small positive constant to ensure that $\text{Id} + \epsilon \mathbf{v}^{(t)}$ is diffeomorphic. We defer the reader to Jena et al. (2026) for the choice of ϵ for maintaining diffeomorphic behavior. The quantity $\mathbf{u}^{(t)} \circ (\text{Id} + \mathbf{v}^{(t)})$ resamples the current warp at locations displaced by $\mathbf{v}^{(t)}$. Optimization proceeds in a coarse-to-fine pyramid; at each level the warp inherits the solution from the previous level, consistent with recommended practice in literature on multi-resolution optimization (Gee et al., 1991; Jena et al., 2026; Avants et al., 2008; Jena et al., 2025). Since diffeomorphisms lie on a Riemannian manifold and admit a group structure, deploying adaptive optimization (that are generally defined for Euclidean spaces) of $\mathbf{v}^{(t)}$ is a non-trivial problem. Jena et al. (2026) also proposes a novel Eulerian descent method for plug-and-play behavior of arbitrary optimizers for diffeomorphic image registration bypassing the need for expensive parallel transport operations by leveraging the group structure of diffeomorphisms.

2.2 Factored Levenberg–Marquardt for Diffeomorphic Registration

Classical LM and the scale problem. For a least-squares residual $\mathbf{r}(\boldsymbol{\theta})$ with Jacobian \mathbf{J} , the LM step solves

$$(\mathbf{J}^\top \mathbf{J} + \lambda \mathbf{I}) \Delta \boldsymbol{\theta} = -\mathbf{J}^\top \mathbf{r}, \quad (3)$$

with $\lambda \geq 0$ the damping parameter. For $\lambda = 0$ this is the Gauss–Newton step; as $\lambda \rightarrow \infty$ the step shrinks toward $-\mathbf{g}/\lambda$, recovering gradient descent. For image registration, we typically optimize a single scalar loss function (ignoring regularization terms) $\mathcal{L}(\mathbf{u})$ which does not necessarily admit a squared loss form required for LM. However, one can convert the problem into a least-squares form by rewriting commonly used loss functions in a squared loss form.

1. **Mean Squared Error (MSE):** This is already in a squared loss form.
2. **Local Normalized Cross Correlation (LNCC):** This can be rewritten as a squared loss form by minimizing $(1 - \text{LNCC})^2$ instead of minimizing $-\text{LNCC}$.
3. **Mutual Information (MI):** This can be rewritten as a squared loss form by minimizing $(\log_2(B) - \text{MI})^2$ instead of minimizing $-\text{MI}$, where B is the number of bins for the parzen windowing method. Note that $\log_2(B)$ upper-bounds the discrete mutual information loss, so the squared loss function will always maximize the mutual information as well.

Therefore, we only have a single scalar residual $r(\mathbf{u})$ (abbreviated as r for brevity) and the Jacobian $\mathbf{J}(\mathbf{u})$ is a vector of the same length as the displacement field (and is actually the gradient of the loss function with respect to the displacement field). Forming $\mathbf{J}^\top \mathbf{J}$ for a 3D displacement field with more than $\sim 10^7$ parameters is intractable.

Rank-1 factorization per voxel. The key observation is that the registration gradient $\mathbf{g} \in \mathbb{R}^{H \times W \times D \times d}$ at each voxel \mathbf{x} depends primarily on *local* image content. We therefore approximate the Gauss–Newton Hessian *independently per voxel* by the rank-1 outer product $\hat{\mathbf{H}}_{\mathbf{x}} = \mathbf{g}_{\mathbf{x}} \mathbf{g}_{\mathbf{x}}^\top$. The damped inverse of this 3×3 matrix has a closed form (proof in Section A):

$$\Delta \mathbf{u}_{\mathbf{x}} = -\frac{r \mathbf{g}_{\mathbf{x}}}{\|\mathbf{g}_{\mathbf{x}}\|^2 + \lambda}. \quad (4)$$

This is the *pointwise update* (denoted as `tile_size=1` in our implementation): it normalizes each voxel’s gradient step by its magnitude, preserving direction while suppressing updates at voxels with small, unreliable gradients. No matrix storage or inversion is required beyond a scalar norm computation.

For richer spatial context, one can pool rank-1 approximations over a window of $(2w + 1)^d$ voxels (where w is the radius of the window, and d is the dimension of the displacement field) to obtain a $d \times d$ positive semi-definite $\hat{\mathbf{H}}_{\text{tile}}$, then apply

$$\Delta \mathbf{u}_{\mathbf{x}} = -(\hat{\mathbf{H}}_{\text{tile}} + \lambda \mathbf{I})^{-1} r \mathbf{g}_{\mathbf{x}}, \quad (5)$$

with the 3×3 inverse computed via `torch.linalg.inv`. In practice, `tile_size=1` matches or exceeds larger tiles at lower cost (Section 3).

Adaptive damping. We adapt λ after each step by comparing successive losses:

$$\lambda^{(t)} = \begin{cases} \mu^+ \cdot \lambda^{(t-1)} & \text{if } \mathcal{L}^{(t)} > \mathcal{L}^{(t-1)} \quad (\text{bad step}), \\ \mu^- \cdot \lambda^{(t-1)} & \text{otherwise} \quad (\text{good step}), \end{cases} \quad (6)$$

with $\mu^+ > 1$ and $0 < \mu^- < 1$. This is a simple heuristic for trust-region-based algorithms. The LM step $\Delta \mathbf{u}$ is then normalized by the same choice of ϵ as in Jena et al. (2026) and integrated via Eq. equation 2.

LM with Rejection Criterion. Since LM is a trust-region-based algorithm, we also implement an LM variant with a rejection criterion. Ranganathan (2004) proposed a rejection criterion based on a quadratic model of the loss function, which can be expensive for large displacement fields. We implement a simpler rejection criterion that computes the quantity

$$\varrho_k = \frac{\mathcal{L}^{(k)} - \mathcal{L}^{(k-1)}}{\|\mathcal{L}^{(k-1)} - \mathcal{L}^{(k-2)}\|} \quad (7)$$

and rejects the step if $\varrho_k > 1$, increases λ according to Equation (6) and retries the step with the incremented λ . Intuitively, if the loss decreases, then ϱ_k is negative, and we always accept the step. We reject the step only if the loss degrades by more than the previous step’s improvement (or tolerable degradation from the previous step). This heuristic requires only the previous two loss values to be stored, and is computationally inexpensive.

2.3 Connections to the Demons Algorithm

The Demons algorithm of Thirion and its diffeomorphic extension (Vercauteren et al., 2009) can be recovered as a special case of per-voxel LM applied to MSE. For MSE loss, the per-voxel residual is $r_{\mathbf{x}} = f(\mathbf{x}) - m(\mathbf{x} + \mathbf{u})$ and the Jacobian of this scalar residual with respect to $\mathbf{u}_{\mathbf{x}}$ is $\mathbf{J}_{\mathbf{x}} = -\nabla m(\mathbf{x} + \mathbf{u})^\top$. The *Gauss–Newton* Hessian at voxel \mathbf{x} is therefore $\hat{\mathbf{H}}_{\mathbf{x}}^{\text{GN}} = \mathbf{J}_{\mathbf{x}}^\top \mathbf{J}_{\mathbf{x}} = \mathbf{n}_{\mathbf{x}} \mathbf{n}_{\mathbf{x}}^\top$, where $\mathbf{n}_{\mathbf{x}} = \nabla m(\mathbf{x} + \mathbf{u})$. Applying the Sherman–Morrison formula to the damped system $(\mathbf{n}_{\mathbf{x}} \mathbf{n}_{\mathbf{x}}^\top + \lambda_{\mathbf{x}} \mathbf{I}) \Delta \mathbf{u}_{\mathbf{x}} = r_{\mathbf{x}} \mathbf{n}_{\mathbf{x}}$ yields exactly

$$\Delta \mathbf{u}_{\mathbf{x}} = \frac{r_{\mathbf{x}} \mathbf{n}_{\mathbf{x}}}{\|\mathbf{n}_{\mathbf{x}}\|^2 + \lambda_{\mathbf{x}}}, \quad (8)$$

Table 1: Optimizer comparison across four registration benchmarks. Mean Dice (\uparrow) for LUMIR, OASIS, Abdomen-L2R; mean TRE in mm (\downarrow) for NLST. “Pairs won” counts image pairs where the method beats Adam. Best result per dataset in **bold**.

Dataset	Method	Mean	Std
LUMIR (Dice \uparrow)	Adam	0.8650	0.0201
	Levenberg-Marquardt	0.8715	0.0163
OASIS (Dice \uparrow)	Adam	0.8028	0.0333
	Levenberg-Marquardt	0.8293	0.0313
NLST (TRE \downarrow)	Adam	0.85	0.28
	Levenberg-Marquardt	1.68	2.16
Abdomen-L2R (Dice \uparrow)	Adam	0.7609	0.1495
	Levenberg-Marquardt	0.7615	0.1516

which is the Demons “active forces” update with $\lambda_{\mathbf{x}} = \alpha^2 r^2$. A key difference is that Demons uses an ‘automatic’, spatially varying, and residual-dependent damping $\lambda_{\mathbf{x}} = \alpha^2 r^2$ chosen to regularize the optical-flow equation, whereas our global λ is adapted across iterations via the trust-region rule of Equation (6). Furthermore, the Demons algorithm uses a ‘per-pixel’ residual term $r_{\mathbf{x}}$ instead of a global residual r . Finally, while Demons is defined specifically for MSE, our formulation generalizes to other similarity metrics through the squared-loss reparameterizations in Section 2.2, enabling second-order acceleration for a broader class of similarity metrics. However, the resemblance of the analytical form of the Demons algorithm to our LM formulation hints at theoretical connections between the two methods, which we leave for future work.

3 Experiments and Results

We evaluate on four publicly available benchmarks using FireANTs with **GreedyRegistration** and FusedCC similarity, comparing **Adam** (baseline, $\beta_1 = 0.9$, $\beta_2 = 0.999$), and **Levenberg-Marquardt** ($\lambda_0 = 0.006$, $\mu^+ = 1.5$, $\mu^- = 0.975$). Benchmarks span brain MRI (LUMIR (Chen et al., 2024), 38 pairs; OASIS (Marcus et al., 2010), 19 pairs), lung CT (NLST (National Lung Screening Trial Research Team, 2011), 10 pairs), and cross-modal abdominal MR \rightarrow CT (Abdomen-L2R (Hering et al., 2022), 48 pairs). Since LUMIR is an unsupervised dataset, we use SynthSeg to generate automated segmentation masks delineating 35 cortical and subcortical structures. We report mean Dice (\uparrow) for segmentation benchmarks and mean Target Registration Error in mm (\downarrow) for NLST.

3.1 Main Results

Table 1 summarizes the comparison. On LUMIR, LM outperforms Adam (0.8715 vs. 0.8650), with performance per pair improving on 36/38 pairs, including a higher worst-case Dice (0.8304 vs. 0.8066), indicating improved robustness. OASIS shows a similar trend: LM achieves 0.8293 against Adam’s 0.8028, a gap of +0.027. On Abdomen-L2R, LM essentially matches Adam (0.7615 vs. 0.7609) across all four organ labels (Table 2). NLST is the exception: Adam (0.85 mm TRE) remains ahead, with LM reaching 1.68 mm. However, we note that the average TRE is inflated by a single outlier pair, and excluding it, LM achieves 0.95 mm versus Adam’s 0.83 mm. The performance improvement of LM is significantly pronounced for brain datasets, but does not degrade performance on other organ systems.

3.2 The Damping Cliff: Sensitivity Analysis of LM Hyperparameters

We select the default LM hyperparameters ($\lambda_0 = 0.006$, $\mu^+ = 1.5$, $\mu^- = 0.975$) via a Bayesian optimization search (Optuna, 50 trials) on LUMIR, starting from these initial values. To confirm generality, we repeated independent Optuna searches on all four benchmarks (OASIS, NLST, Abdomen-L2R); in every case the

Table 2: Per-label Dice on Abdomen-L2R (4 organs, 48 pairs). LM performs similarly to Adam across all labels.

Label	Adam	LM
Spleen	0.8344	0.8325
Right kidney	0.7288	0.7211
Left kidney	0.7594	0.7662
Liver	0.7208	0.7262

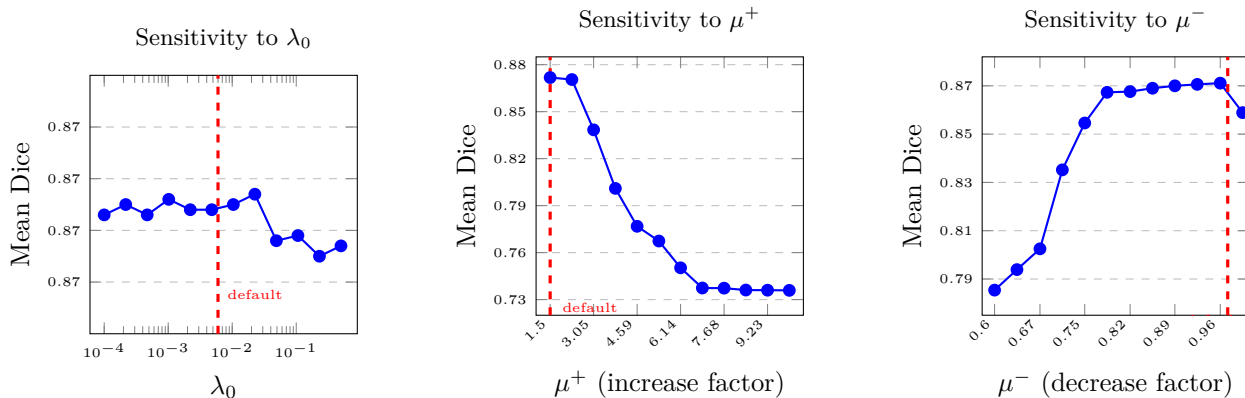


Figure 1: Sensitivity of mean Dice on LUMIR (38 pairs) to all three LM hyperparameters. Our defaults ($\lambda_0 = 0.006$, $\mu^+ = 1.5$, $\mu^- = 0.975$, red dashed) were selected via Bayesian optimization on LUMIR and are marked in each panel. **Left:** λ_0 is entirely insensitive—Dice varies by < 0.001 over a $5000\times$ range. **Center:** μ^+ has a catastrophic cliff between 2.3 and 3.0; our default of 1.5 sits at the safe peak. **Right:** μ^- shows monotone improvement up to 0.963 then a small drop; our default of 0.975 sits in the optimal plateau.

search converges to nearly identical configurations ($\mu^+ \in [1.5, 2.0]$, $\mu^- \approx 0.97\text{--}0.98$), confirming that these are properties of the optimizer–task interaction rather than dataset-specific artifacts (see also Section 3.3).

Figure 1 shows a sweep of all three hyperparameters on LUMIR, with the remaining parameters fixed to their defaults.

λ_0 is entirely insensitive. Dice varies by less than 0.001 across a $5000\times$ range ($\lambda_0 \in [10^{-4}, 0.5]$), because the adaptive schedule in Eq. equation 6 rapidly moves λ away from any initial value within the first few iterations. The default of 0.006 is representative, but any value in this range is equally valid.

A catastrophic cliff in μ^+ . Dice stays above 0.870 for $\mu^+ \leq 2.27$, then collapses by -0.033 between 2.3 and 3.0, and saturates near 0.736 above 3.8; no better than identity. Our default of $\mu^+ = 1.5$ lies at the safe peak of this curve, yielding the best observed Dice of 0.872. The mechanism is self-amplifying: a large increase factor aggressively overdamps on any bad step, driving λ upward until every subsequent update is near-zero. The safe operating range spans only $\mu^+ \in [1.5, 2.3]$ across all datasets.

Moderate, monotone sensitivity of μ^- . Dice increases monotonically from 0.785 at $\mu^- = 0.6$ to 0.871 at $\mu^- = 0.963$, then drops slightly at $\mu^- = 0.999$. Our default of 0.975 sits near the top of this plateau, yielding 0.871. Too small a decrease factor drops λ too quickly after good steps, overcommitting to Newton-like steps before the curvature estimate is reliable.

Tile size. The LM Hessian approximation can pool over spatial tiles of side k , forming a $d \times d$ local covariance matrix instead of the rank-1 per-voxel outer product. Figure 2 sweeps $k = 1 \dots 10$ on all 38 LUMIR pairs with all other hyperparameters fixed to their defaults. Pointwise updates ($k = 1$) achieve the

best mean Dice (0.8716) and lowest standard deviation (0.017); performance drops by -0.009 at $k = 2$ and degrades roughly monotonically to 0.828 at $k = 7-10$, with standard deviation rising throughout. Aggregating over a neighbourhood blurs the per-voxel curvature signal, producing a spatially inconsistent step size that hurts convergence; we therefore fix $k = 1$ for all experiments.

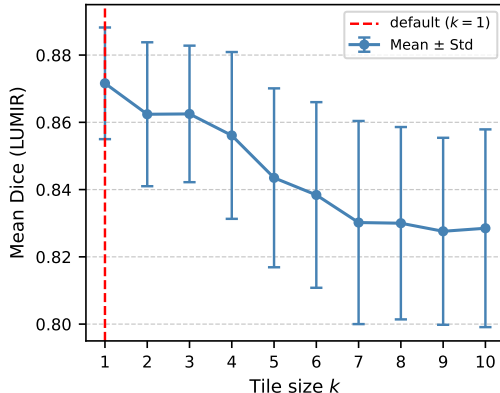


Figure 2: Mean Dice (\pm std) on LUMIR (38 pairs) as tile size k varies from 1 to 10, with all other LM hyperparameters fixed to their defaults. Pointwise updates ($k=1$, red dashed) achieve the best mean Dice (0.8716) and lowest variance; performance drops -0.009 at $k=2$ and degrades monotonically to 0.828 by $k=7-10$, with standard deviation rising throughout.

Table 3: Cross-dataset transfer of LUMIR-tuned LM hyperparameters compared to per-dataset Optuna search. “LM-transfer” applies LUMIR parameters directly with no additional tuning; “LM-tuned” uses dataset-specific search.

Dataset	Adam	LM-transfer	LM-tuned
LUMIR (Dice)	0.8650	—	0.8715
OASIS (Dice)	0.8028	0.8289	0.8293
NLST (TRE, mm)	0.85	1.68 [‡]	1.68
Abdomen (Dice)	0.7609	0.7615	0.7615

[‡] Inflated by one outlier pair; excluding it: 0.95 mm vs. 0.83 mm for Adam.

3.3 Hyperparameter Transfer and Universality

A practical concern for any optimizer is whether its hyperparameters must be re-tuned per dataset. They do not: the optimal LM configuration from LUMIR ($\lambda_0 = 0.006$, $\mu^+ = 1.5$, $\mu^- = 0.975$, `tile_size=1`) transfers directly to OASIS, NLST, and Abdomen-L2R without modification (Table 3). Independent Optuna searches on each target dataset converge to nearly identical configurations ($\mu^+ \in [1.5, 2.0]$, $\mu^- \approx 0.97-0.98$), confirming that these are properties of the optimizer–task interaction rather than dataset-specific artifacts.

3.4 Step Rejection and Damping Cap

The adaptive damping rule (Equation (6)) increases λ after any bad step, but does not *undo* the step itself. A natural extension is to additionally restore the warp and retry with increased damping when the loss degrades beyond a threshold. Concretely, a step is rejected if

$$\mathcal{L}^{(t)} - \mathcal{L}^{(t-1)} > \tau \cdot |\mathcal{L}^{(t-1)} - \mathcal{L}^{(t-2)}|, \quad (9)$$

with tolerance ratio τ . On rejection the warp is restored, λ is multiplied by μ^+ , and the step is retried up to 10 times. A critical safeguard is a cap λ_{\max} : without it, repeated rejections drive λ to infinity, collapsing every subsequent update to near-zero.

Table 4: Effect of step rejection on default LM. All conditions use $\tau = 1.0$. Without a cap, rejection is consistently harmful across all datasets. With $\lambda_{\max} = 1.0$, rejection is dataset-dependent: neutral on LUMIR and OASIS, mildly harmful on Abdomen-L2R (48 pairs), and beneficial on NLST by suppressing one catastrophic outlier. Best result per dataset in **bold**.

Dataset	Condition	Mean	Std
LUMIR (Dice \uparrow)	No rejection	0.8715	0.0163
	+ rejection, cap = ∞	0.8654	0.0303
	+ rejection, cap = 1.0	0.8709	0.0170
OASIS (Dice \uparrow)	No rejection	0.8028	0.0333
	+ rejection, cap = ∞	0.7362	0.0899
	+ rejection, cap = 1.0	0.8014	0.0343
Abdomen-L2R (Dice \uparrow)	No rejection	0.7615	0.1516
	+ rejection, cap = 1.0	0.7508	0.1529
NLST (TRE mm \downarrow)	No rejection	1.679	2.165
	+ rejection, cap = 1.0	1.632	0.593

We ablate two settings ($\tau = 1.0$, cap = 1.0 vs. no cap) across all four datasets using the default LM config. Table 4 reports the results. The uncapped case is consistently harmful across all four datasets, mirroring the runaway λ phenomenon seen with large μ^+ . On LUMIR, removing the cap costs -0.006 Dice and nearly doubles standard deviation (std 0.030 vs. 0.016); on OASIS the drop is -0.067 with standard deviation nearly tripling (std 0.090 vs. 0.033). Capping at $\lambda_{\max} = 1.0$ eliminates this failure mode in all cases.

With the cap, outcomes are dataset-dependent. On LUMIR and OASIS, rejection is effectively neutral (-0.0006 and -0.0014 Dice, respectively). On Abdomen-L2R (48 cross-modal pairs), rejection is mildly harmful (-0.011 Dice; winning only 11/48 pairs). We find that the rejection mechanism is overly conservative on these harder cross-modal pairs, repeatedly rejecting useful steps and slowing convergence.

NLST presents the most interesting case. Rejection with $\lambda_{\max} = 1.0$ reduces mean TRE from 1.68 to 1.63 mm, but the primary driver is outlier suppression: one pair drops from 8.16 to 2.75 mm while 9 of 10 pairs slightly regress ($+0.11$ – 1.63 mm). The rejection mechanism trades a small average regression for a dramatic worst-case improvement, reflecting that the outlier pair had a genuinely ill-conditioned step that rejection correctly identifies and dampens.

Recommendation. The cap λ_{\max} is essential and prevents catastrophic divergence in all cases. Whether to enable rejection ($\tau = 1.0$, $\lambda_{\max} = 1.0$) is dataset-dependent: it is beneficial when outlier robustness is the priority (e.g. NLST), and neutral or mildly harmful otherwise. We disable it by default to provide good asymptotic convergence on average and have enabled robust defaults for the rejection criterion if worst-case cost minimization is desired.

3.5 Memory and Runtime

Table 5 confirms the theoretical memory advantage. Because LM carries no moment buffers, it saves 11–25% peak GPU memory depending on volume size, and is never slower than Adam. The speedup is most pronounced at small volumes ($1.67\times$ at $N = 64$, where Adam’s moment-update overhead dominates) and narrows to $\sim 4\%$ at larger N where both methods are compute-bound. At $N = 512$, LM saves $\approx 3,024$ MB.

4 Discussion

We discuss a few implications of our experiments and findings.

When does LM help? The per-voxel Hessian approximation is most reliable for *in-vivo* brain MRI registration, where the structures of interest have reasonable contrast and have a huge variability in shape (i.e.

Table 5: Peak GPU memory (MB) and time per step (s) on an NVIDIA A6000, for cubic volumes of side N . LM is never slower and consistently uses less memory. Best result in **bold**.

N	Peak memory (MB)			Time/step (s)		
	Adam	LM	Mem. saved	Adam	LM	Speedup
64	61.1	55.9	8.6%	0.593	0.356	1.67×
128	433.1	384.9	11.1%	0.605	0.606	1.00×
192	1444.1	1282.7	11.2%	1.085	1.062	1.02×
256	3400.1	3022.1	11.1%	2.127	2.061	1.03×
320	6638.1	5898.0	11.1%	3.937	3.801	1.04×
384	5192.1	3916.4	24.6%	6.161	5.936	1.04×
448	8246.1	6218.3	24.6%	9.730	9.328	1.04×
512	12296.1	9272.1	24.6%	14.484	13.952	1.04×

laminar and curvilinear structures like the cortex, white matter, and sulcal CSF, and amoeboid structures like the ventricles, caudate nucleus, and putamen). In noisier and sparser settings (cross-modal Abdomen-L2R, highly deformed lung CT), Adam’s momentum provides robustness that the LM estimate cannot match on the hardest pairs.

Rehabilitating second-order methods. The most striking finding is not that LM is better in aggregate, but that the optimizer harbors a sharp, self-amplifying failure mode in its damping schedule. Dice remains above 0.870 for $\mu^+ \leq 2.27$, then collapses by -0.033 between 2.3 and 3.0, eventually saturating near 0.736 which is only slightly better than the identity warp. A large increase factor aggressively overdamps on any bad step, driving λ upward until every subsequent update is near-zero, locking the warp in place. The safe operating range is narrow: $\mu^+ \in [1.5, 2.3]$ across all four datasets, and an uncapped step-rejection mechanism produces the same runaway behaviour.

Recommended configuration. Based on our sensitivity analysis and cross-dataset transfer experiments, we recommend the following universal LM settings for diffeomorphic registration:

λ_0	0.01	(insensitive; any value in $[10^{-4}, 0.5]$ works)
μ^+	1.5	(<i>critical</i> : must stay < 2.3)
μ^-	0.975	(keep in $[0.78, 0.97]$)
tile_size	1	(pointwise; lower cost, no accuracy loss)

These parameter settings are implemented as the default configuration in the FireANTs implementation.

5 Conclusion

We introduced a factored Levenberg–Marquardt optimizer for diffeomorphic image registration in FireANTs, built on a per-voxel rank-1 Hessian approximation that makes second-order updates computationally competitive with Adam. The central insight is a *damping cliff*: the increase factor μ^+ must be kept below 2.3 or registration collapses. With a corrected configuration tunable from a single dataset and transferable across modalities, LM matches or outperforms Adam on three of four benchmarks while using less memory. We hope this encourages registration on larger datasets owing to the availability of an efficient, trust-region based adaptive optimizer without sacrificing performance.

References

Brian B Avants, Charles L Epstein, Murray Grossman, and James C Gee. Symmetric diffeomorphic image registration with cross-correlation: evaluating automated labeling of elderly and neurodegenerative brain. *Medical image analysis*, 12(1):26–41, 2008.

-
- Junyu Chen, Yuankai Huo, et al. LUMIR: Learn2reg 2024 unimodal brain MRI registration challenge. <https://learn2reg.grand-challenge.org/>, 2024. Learn2Reg 2024 Challenge.
- James C Gee, Martin Reivich, L Bilaniuk, David Hackney, R Zimmerman, Stanislav Kovacic, and Ruzena K Bajcsy. Evaluation of multiresolution elastic matching using mri data. In *Medical Imaging V: Image Processing*, volume 1445, pp. 226–234. SPIE, 1991.
- Alessa Hering, Lasse Hansen, Tony C. W. Mok, Albert C. S. Chung, Hanna Siebert, Stephanie Häger, Annkristin Lange, Marco Lorenzi, Bartłomiej W. Burton, Enzo Ferrante, et al. Learn2Reg: Comprehensive multi-task medical image registration challenge, dataset and evaluation in the era of deep learning. In *IEEE Transactions on Medical Imaging*, volume 42, pp. 697–712, 2022. doi: 10.1109/TMI.2022.3213983.
- Rohit Jena, Pratik Chaudhari, and James C Gee. Deep implicit optimization enables robust learnable features for deformable image registration. *Medical Image Analysis*, 103:103577, 2025.
- Rohit Jena, Pratik Chaudhari, and James C. Gee. FireANTs: Adaptive riemannian optimization for multi-scale diffeomorphic registration. *Nature Communications*, 2026. URL <https://arxiv.org/abs/2404.01249>.
- Diederik P. Kingma and Jimmy Ba. Adam: A method for stochastic optimization. In *International Conference on Learning Representations (ICLR)*, 2015. URL <https://arxiv.org/abs/1412.6980>.
- Kenneth Levenberg. A method for the solution of certain non-linear problems in least squares. *Quarterly of Applied Mathematics*, 2(2):164–168, 1944. doi: 10.1090/qam/10666.
- Dong C Liu and Jorge Nocedal. On the limited memory bfgs method for large scale optimization. *Mathematical programming*, 45(1):503–528, 1989.
- Daniel S. Marcus, Anthony F. Fotenos, John G. Csernansky, John C. Morris, and Randy L. Buckner. Open access series of imaging studies (OASIS): Longitudinal MRI data in nondemented and demented older adults. *Journal of Cognitive Neuroscience*, 22(12):2677–2684, 2010. doi: 10.1162/jocn.2009.21407.
- Donald W. Marquardt. An algorithm for least-squares estimation of nonlinear parameters. *Journal of the Society for Industrial and Applied Mathematics*, 11(2):431–441, 1963. doi: 10.1137/0111030.
- National Lung Screening Trial Research Team. Reduced lung-cancer mortality with low-dose computed tomographic screening. *New England Journal of Medicine*, 365(5):395–409, 2011. doi: 10.1056/NEJMoa1102873.
- Ananth Ranganathan. The levenberg-marquardt algorithm. *Tutorial on LM algorithm*, 11(1):101–110, 2004.
- Jean-Philippe Thirion. Image matching as a diffusion process: an analogy with Maxwell’s demons.
- Tom Vercauteren, Xavier Pennec, Aymeric Perchant, and Nicholas Ayache. Diffeomorphic demons: Efficient non-parametric image registration. *NeuroImage*, 45(1 Suppl):S61–S72, 2009. doi: 10.1016/j.neuroimage.2008.10.040.

A Proof of the Factored Levenberg–Marquardt Update

We derive the closed-form pointwise update in Equation (4) from the classical LM linear system in Equation (3).

Setup. As argued in Section 2.2, for a scalar residual $r(\mathbf{u})$ the global Jacobian is the gradient vector $\mathbf{J} = \nabla_{\mathbf{u}} L \in \mathbb{R}^{H \times W \times D \times 3}$. At each voxel \mathbf{x} , we approximate the Gauss–Newton Hessian *independently* by the rank-1 outer product of the local gradient:

$$\hat{\mathbf{H}}_{\mathbf{x}} = \mathbf{J}_{\mathbf{x}} \mathbf{J}_{\mathbf{x}}^{\top} = \mathbf{g}_{\mathbf{x}} \mathbf{g}_{\mathbf{x}}^{\top} \in \mathbb{R}^{3 \times 3}. \quad (10)$$

Substituting into Equation (3) for the local 3-vector $\Delta \mathbf{u}_{\mathbf{x}}$ gives

$$(\mathbf{g}_{\mathbf{x}} \mathbf{g}_{\mathbf{x}}^{\top} + \lambda \mathbf{I}) \Delta \mathbf{u}_{\mathbf{x}} = -r \mathbf{g}_{\mathbf{x}}, \quad (11)$$

where the right-hand side $-\mathbf{J}_{\mathbf{x}}^{\top}$ reduces to $-\mathbf{g}_{\mathbf{x}}$.

Sherman–Morrison inverse. The Sherman–Morrison formula states that for an invertible matrix $\mathbf{A} \in \mathbb{R}^{n \times n}$ and vectors $\mathbf{u}, \mathbf{v} \in \mathbb{R}^n$ with $1 + \mathbf{v}^{\top} \mathbf{A}^{-1} \mathbf{u} \neq 0$,

$$(\mathbf{A} + \mathbf{u} \mathbf{v}^{\top})^{-1} = \mathbf{A}^{-1} - \frac{\mathbf{A}^{-1} \mathbf{u} \mathbf{v}^{\top} \mathbf{A}^{-1}}{1 + \mathbf{v}^{\top} \mathbf{A}^{-1} \mathbf{u}}. \quad (12)$$

We apply this with $\mathbf{A} = \lambda \mathbf{I}$, $\mathbf{u} = \mathbf{g}_{\mathbf{x}}$, $\mathbf{v} = \mathbf{g}_{\mathbf{x}}$:

$$\begin{aligned} (\lambda \mathbf{I} + \mathbf{g}_{\mathbf{x}} \mathbf{g}_{\mathbf{x}}^{\top})^{-1} &= \frac{1}{\lambda} \mathbf{I} - \frac{\frac{1}{\lambda} \mathbf{g}_{\mathbf{x}} \mathbf{g}_{\mathbf{x}}^{\top} \frac{1}{\lambda}}{1 + \mathbf{g}_{\mathbf{x}}^{\top} \frac{1}{\lambda} \mathbf{g}_{\mathbf{x}}} \\ &= \frac{1}{\lambda} \mathbf{I} - \frac{\mathbf{g}_{\mathbf{x}} \mathbf{g}_{\mathbf{x}}^{\top}}{\lambda(\lambda + \|\mathbf{g}_{\mathbf{x}}\|^2)}. \end{aligned} \quad (13)$$

Deriving the update. Solving Equation (11) gives $\Delta \mathbf{u}_{\mathbf{x}} = -(\mathbf{g}_{\mathbf{x}} \mathbf{g}_{\mathbf{x}}^{\top} + \lambda \mathbf{I})^{-1} r \mathbf{g}_{\mathbf{x}}$. Substituting Equation (13) and using $\mathbf{g}_{\mathbf{x}}^{\top} \mathbf{g}_{\mathbf{x}} = \|\mathbf{g}_{\mathbf{x}}\|^2$:

$$\begin{aligned} \Delta \mathbf{u}_{\mathbf{x}} &= - \left[\frac{1}{\lambda} \mathbf{I} - \frac{\mathbf{g}_{\mathbf{x}} \mathbf{g}_{\mathbf{x}}^{\top}}{\lambda(\lambda + \|\mathbf{g}_{\mathbf{x}}\|^2)} \right] \mathbf{g}_{\mathbf{x}} r \\ &= - \frac{\mathbf{g}_{\mathbf{x}} r}{\lambda} + \frac{\mathbf{g}_{\mathbf{x}} r \|\mathbf{g}_{\mathbf{x}}\|^2}{\lambda(\lambda + \|\mathbf{g}_{\mathbf{x}}\|^2)} \\ &= \frac{\mathbf{g}_{\mathbf{x}} r}{\lambda} \left[-1 + \frac{\|\mathbf{g}_{\mathbf{x}}\|^2}{(\lambda + \|\mathbf{g}_{\mathbf{x}}\|^2)} \right] \\ &= \frac{\mathbf{g}_{\mathbf{x}} r}{\lambda} \cdot \frac{-(\lambda + \|\mathbf{g}_{\mathbf{x}}\|^2) + \|\mathbf{g}_{\mathbf{x}}\|^2}{(\lambda + \|\mathbf{g}_{\mathbf{x}}\|^2)} \\ &= - \frac{\mathbf{g}_{\mathbf{x}} r}{\|\mathbf{g}_{\mathbf{x}}\|^2 + \lambda}, \end{aligned} \quad (14)$$

which is Equation (4). □